

PAPER • OPEN ACCESS

Particle stabilised high internal phase emulsion scaffolds with interconnected porosity facilitate cell migration

To cite this article: Areli Munive-Olarte *et al* 2025 *Biomed. Mater.* **20** 065005

View the [article online](#) for updates and enhancements.

You may also like

- [Shortwave infrared imaging-guided radiosensitization using rare-earth-doped nanoparticles delivered via microneedles for enhanced melanoma therapy](#)
Mohd Yaqub Khan, Jen-Kun Chen, Lokesh Agrawal et al.
- [Black phosphorus nanosheets in orthopedics: from material fabrications to therapeutic prospects](#)
Yong Sun, Yizhi Zhang, Ziyang Wei et al.
- [Antimicrobial self-healing injectable hydrogels based on chitosan, collagen, and polyvinyl alcohol for chronic wound treatment](#)
Lorena Duarte-Peña, Sheila I Peña-Corona, Luis E López-Jácome et al.



GAS

BreathSpec®



The combination of GC and IMS enables a physical separation to detect volatiles without pre-concentration directly sampled from human breath.

Our GC-IMS based analyzer allows instant breath sampling and analysis of volatiles in minutes.



The transportable GC-IMS facilitates versatile sampling incl. direct exhalation, syringe based and also gas bags for sampling of breath and static body headspace (oral/nasal/skin).

▶▶▶ [click for more details](#)



PAPER

OPEN ACCESS

RECEIVED
27 June 2025REVISED
14 August 2025ACCEPTED FOR PUBLICATION
10 September 2025PUBLISHED
6 October 2025

Original content from
this work may be used
under the terms of the
Creative Commons
Attribution 4.0 licence.

Any further distribution
of this work must
maintain attribution to
the author(s) and the title
of the work, journal
citation and DOI.



Particle stabilised high internal phase emulsion scaffolds with interconnected porosity facilitate cell migration

Areli Munive-Olarte^{1,2} , Enes Durgut³ , Stefaan W Verbruggen⁴ , Frederik Claeysens^{1,2} and Gwendolen C Reilly^{1,2,*}

¹ Kroto Research Institute, School of Chemical, Materials and Biological Engineering, University of Sheffield, Sheffield, United Kingdom

² INSIGNEO Institute for in Silico Medicine, School of Chemical, Materials and Biological Engineering, University of Sheffield, Sheffield, United Kingdom

³ Department of Genetics and Bioengineering, Alanya Alaaddin Keykubat University, Alanya, Turkey

⁴ Centre for Predictive *in-vitro* models and Centre for Bioengineering, School of Engineering and Materials Science, Queen Mary University of London, London, United Kingdom

* Author to whom any correspondence should be addressed.

E-mail: g.reilly@sheffield.ac.uk

Keywords: bone scaffold, pore interconnectivity, cell infiltration, osteogenic differentiation, tissue engineering

Abstract

A key challenge in bone tissue engineering (BTE) is designing structurally supportive scaffolds, mimicking the native bone matrix, yet also highly porous to allow nutrient diffusion, cell infiltration, and proliferation. This study investigated the effect of scaffold interconnectivity on human bone marrow stromal cell (BMSC) behaviour. Highly interconnected, porous scaffolds (polyHIPEs) were fabricated using the emulsion templating method from 2-ethylhexyl acrylate/isobornyl acrylate (IBOA) and stabilised with ~200 nm IBOA particles. Pore interconnectivity was tuned by varying the internal phase fraction from 75%–85% and characterised by the degree of openness, Euler number, frequency, and size of pore interconnects. The attachment, proliferation, infiltration, and osteogenic differentiation of the BMSC cell line (Y201) were evaluated on these scaffolds. Results showed that high pore interconnectivity facilitated diffusion and cell infiltration throughout the scaffolds. Furthermore, the most interconnected scaffolds enhanced osteogenic differentiation of Y201 cells, as evidenced by elevated alkaline phosphatase activity and increased calcium and collagen production compared to less interconnected scaffolds. These findings emphasise the importance of scaffold interconnectivity in BTE for efficient nutrient transport, facilitating cell migration and infiltration, and supporting the development of interconnected cell networks that positively influence osteogenic differentiation.

1. Introduction

Bone tissue engineering (BTE) seeks to promote bone regeneration by combining biomaterials, bone progenitor cells, and growth factors synergistically. Biomaterials serve as scaffolds to support cell proliferation and bone extracellular matrix formation. Whether used as bone graft substitutes or *in-vitro* models, scaffolds require a three-dimensional (3D) porous architecture that facilitates cell infiltration and effective nutrient solute transport [1].

Characteristics like pore size, porosity, and pore interconnectivity are structural features that affect cell mechanobiology, influencing cell attachment, growth, cell migration, vascularisation, and

nutrient-waste exchange [2, 3]. There is no consensus about the optimal pore size for scaffolds in BTE, but small pores can reduce cell migration and fluid flow, while large pores may reduce the available surface area, limiting cell attachment [2, 4]. Moreover, mesenchymal stem cells (MSCs) in confined areas with low contractibility favour an adipogenic fate, whereas larger spaces are more likely to support an osteogenic lineage [5]. A high porosity in scaffolds is desired because of the higher surface area, providing more space for cells to attach, migrate, grow, and interact. *In-vitro* studies using scaffolds with 70% or greater porosity supported better bone ingrowth and osteogenic differentiation [6]. Generally, high porosity correlates with high

permeability within a scaffold. However, scaffolds with similar pore size and porosity can have different permeabilities [7]. This is because a high porosity alone does not always describe how accessible and interconnected the pores are. A more comprehensive assessment of scaffold openness includes factors such as permeability, porosity, pore size, pore interconnectivity, and the dimensions and distribution of pore interconnects [8]. Some of the methods for calculating these parameters on scaffolds include scanning electron microscopy (SEM) [9], mercury intrusion porosimeter [10], x-ray microcomputed tomography [11], nano-computed tomography [12], permeability measurements [13], permeability simulations [14], or pore volume/surface area measurements [10].

Among the techniques used to produce more open or interconnected scaffolds are 3D printing [15], salt leaching [16], gas foaming [17], freeze-drying [18], porogens [19], and emulsion templated scaffolds [12]. The emulsion templating method enables the production of polymerised emulsions with high internal phase volumes ($\geq 74\%$), (HIPEs). The empty spaces generated by HIPE polymerisation to form polyHIPEs and subsequent water removal are called pores or voids, and the narrow passages that connect those are called pore throats, windows, or interconnects [20].

PolyHIPEs can be fabricated in various shapes using casting techniques, stereolithography, 3D printing, or electrospinning [9]. As emulsions consist of two immiscible liquids, a surfactant or particles are needed to stabilise them. While surfactants reduce the oil-water interfacial tension, particles create a mechanical barrier between the phases. Particle-stabilised polyHIPEs, known as pickering polyHIPEs, or polyHIPPES, offer advantages over surfactant-stabilised ones, including enhanced mechanical properties, permeability, and larger pores [20]. However, pickering polyHIPEs are typically associated with closed pores due to the thick interfacial barrier between the emulsion phases. In a recent study, acrylate particles were used to stabilise HIPEs via arrested coalescence [10]. This mechanism enabled the production of larger pore polyHIPEs with interconnected porosity. Additionally, a tuneable pore size and interconnectivity were achieved by adjusting the volume of the internal phase and the size and concentration of particles. While pore size and porosity of scaffolds have often been compared for their effects on MSC responses, pore interconnectivity has received less attention. Therefore, this study aims to investigate the effect of pore interconnectivity within pickering polyHIPEs on the behaviour of MSCs, focusing on the infiltration and migration into the scaffolds.

2. Materials and methods

2.1. Isobornyl acrylate (IBOA) particle preparation

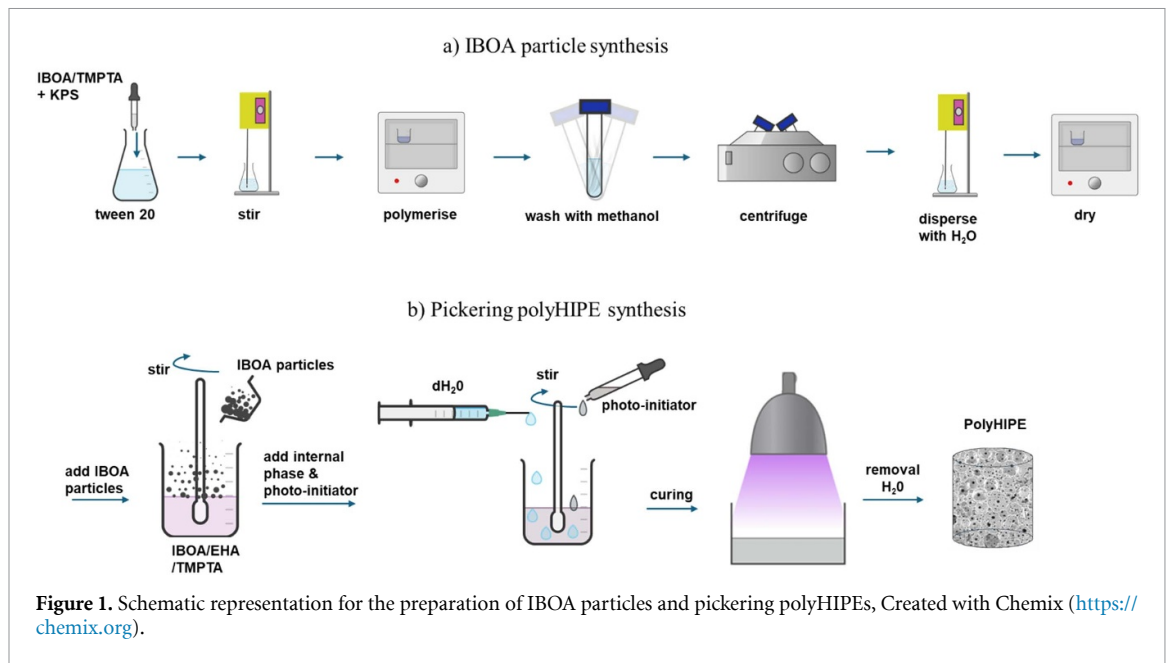
IBOA particles were used to stabilise the HIPEs. Particles around 200 nm were fabricated via the ultrasound-assisted oil-in-water (o/w) emulsion polymerisation method (figure 1) [10]. In brief, per 9 g of the continuous phase, 1 g of the internal phase is used. Both are mixed for 2 min using a sonicator at 100 W, 30 kHz (Hielscher UP100H, Hielscher Ultrasound Technology). The continuous phase consisted of 0.5 wt.% of Tween 20 (P2287, Sigma Aldrich) in deionised water (dH₂O), while the internal phase was a blend of 75 wt.% IBOA (392103, Sigma)/25 wt.% trimethylolpropane triacrylate (TMPTA) (246808, Merck) and 2 wt.% potassium persulfate (216224, 99%, Sigma) as the initiator. The emulsion was polymerised in a convection oven at 65 °C for 18 h. Particles were washed with methanol (99.9%, Fisher, UK) under agitation for 15 min and centrifuged at 4000 rpm for 10 min. Then, the supernatant was replaced with 10 ml of dH₂O and dispersed with a sonicator at 100 W, 30 kHz, for 1 min. Finally, the particles were dried overnight in an oven at 65 °C.

2.2. Fabrication of polyHIPEs

HIPEs were prepared by mixing a 2-ethylhexyl acrylate (EHA) (290815, 98%, Sigma)/IBOA blend with the respective amount of dH₂O for a 75, 80, or 85 (% v/v) internal phase [10]. In detail, the blend was prepared by mixing 63 wt.% EHA, 21 wt.% IBOA, 16 wt.% TMPTA, and 5 wt.% IBOA particles by sonication (100 W, 30 kHz) for 1 min. The corresponding volume of dH₂O was added to the monomer phase at a constant flow rate of 0.8 ml min⁻¹ using a syringe pump (18 mm), while the monomer blend was under agitation using an overhead stirrer (Pro40, SciQuip) at 500 rpm. Subsequently, the photo-initiator, 0.1 g of 2-hydroxy-2-methylpropiophenone (405655, 95%, Sigma) per 4 g of monomer blend, was added. Emulsions were photopolymerised using a belt conveyor ultraviolet curing system (GEW Engineering UV) and dried in an oven at 60 °C for 18 h. Then, polyHIPEs were washed with methanol to remove the uncured monomers. Samples were named according to the %v/v of the internal phase preceding a *H* for HIPEs and a *P* for polyHIPEs. For instance, P75 was a polyHIPE with an internal phase of 75% v/v. All reagents and equipment were kept constant across all groups (P75, P80, P85). Samples from each experimental group were assigned using the lottery method, for polyHIPEs characterisation.

2.3. PolyHIPEs characterisation

PolyHIPE samples were prepared for SEM imaging by first removing outer layers with a scalpel.



Cuboid cross-sections ($1 \times 1 \times 0.5$ mm, $n = 3$ per group) were then cut from these inner regions. Each cross-section was gold-coated and imaged using a SEM (Inspect F, FEI), operated with an acceleration voltage of 15 kV and a spot size of 3.5 in secondary electron mode. Image J (<https://imagej.net/ij/download.html>) was used to measure the diameter of pores ($n = 300$), diameter of pore interconnects, also known as pore throats or windows ($n = 200$), and number of pore interconnects per pore ($n = 50$) from SEM micrographs. For the diameter, around 40 random pores/interconnects were measured from six SEM micrographs for each polyHIPE. A statistical correction factor ($2\sqrt{3}$) was applied, considering the uneven sectioning of the sample [9, 10].

Degree of openness (DOO) is the ratio of the open surface to the total surface of a pore. It was determined in polyHIPEs ($n = 20$) according to equation (1), where A_w is the surface area of the interconnects and A_p is the surface area of the pore [10]. The pore surface was considered the curved surface area of a hemisphere. Image J was used to adjust the threshold to improve pore/interconnects identification and measured using the analyse particles plugin or by measuring the diameters of pores or interconnects.

$$\text{DOO} = \frac{\sum A_w}{A_p}. \quad (1)$$

The porosity and apparent density (ρ) of the polyHIPEs ($n = 3$ per group) were measured by the ethanol displacement method, equations (2) and (3). Dry samples were weighed (W_0) and placed in a known volume of ethanol (99.8%, Fisher) (V_1) for 5 min, then vacuumed to evacuate the air and allow the ethanol to enter the pores of the scaffold. The total

volume of the ethanol impregnated in the scaffold (V_2), the weight of the wet scaffolds (W_1), and the remaining ethanol (V_3) were recorded [21].

$$\text{Porosity (\%)} = \frac{V_1 - V_3}{V_2 - V_3} * 100 \quad (2)$$

$$\rho = \frac{W_0}{V_2 - V_3}. \quad (3)$$

PolyHIPEs were scanned dry using a SkyScan 1272 3D x-ray microscope (Bruker). Imaging parameters included pixel size of $4.0 \mu\text{m}$, a source voltage of 50 kV, and a source current of $200 \mu\text{A}$. Before analysis, the dataset was processed with thresholding, filtering, and despeckle tools using CTAn software (Bruker) to reduce the noise. Euler number was calculated, and 3D visualisations were generated with CTvox software (Bruker).

2.4. Dextran diffusion

PolyHIPEs were cut into 4 mm diameter and 2 mm height using a cork borer. Then their sides were cut off using a scalpel to eliminate any non-porous external layer. Samples were treated in a vacuum plasma cleaner (Zepto, Diener Electronic) at 0.8 mbar with a power of 50 W for 60 s to increase their hydrophilicity [22]. These were stained with 0.3 wt.% Sudan black B (199 664, Sigma) in 70% ethanol, and excess was removed with three washes of phosphate-buffered saline (PBS) (P4417, 1X, Sigma-Aldrich). PolyHIPEs ($n = 3$ per group) were glued (ethyl-2-cyanoacrylate, UHU GmbH & Co.) to petri plates and hydrated with dH_2O for 4 h. dH_2O was removed, and a solution of 0.1 mg ml^{-1} fluorescein isothiocyanate-dextran (FITC-dextran) (FD150, 150 kDa, Sigma) prepared in

PBS was poured into the petri dish until the height of the scaffold [23]. After 15 min, imaging was performed on a confocal fluorescent microscope (Leica SP8 TCS Microscope, UK) at room temperature (RT) using a 488 nm laser and 10X objective. The relative fluorescence intensity was measured using ImageJ software.

2.5. Cell culture

A human telomerase reverse transcriptase immortalised (hTERT) bone marrow stromal cell (BMSC) clonal line Y201 (CVCL_VG68) was used in all experiments. The Y201 line was selected because it maintained a mesenchymal morphology and tripotent differentiation (adipogenic, chondrogenic, and osteogenic) when induced chemically [24]. This clone line was donated by Professor Paul Genever (University of York) under a material transfer agreement. Y201 BMSCs were maintained in basal medium consisting of Dulbecco's Modified Eagle Medium (42430025, LOT# 2605 210, Gibco), supplemented with 10% v/v foetal bovine serum (FBS) (A5256701, LOT# 08Q5283K, Gibco) and 1% v/v (100 I.U ml⁻¹–100 µg ml⁻¹) penicillin-streptomycin (P4333, LOT# 0000137186, Sigma) [25]. Cells were maintained in a humidified incubator at 37 °C and 5% CO₂. Cultures were passaged at 80% confluence using Trypsin-EDTA (T4049, LOT# SLCL2418, Sigma) and frozen down with a cryo-freezing container at –80 °C in 10% v/v dimethyl sulfoxide (D2650, LOT# RNBK3096, Sigma) in FBS for 24 h and later stored in liquid nitrogen until use. A mycoplasma analysis was performed before cell seeding using a mycoplasma detection kit (rep-mysnc-50, InvivoGen).

2.6. Cell seeding

Scaffolds were cut into 7 mm in diameter and 2 mm in height using a cork borer No. 3, and any external layer was removed before with a scalpel. Due to the inherent hydrophobicity of the monomers used, the polyHIPEs surface was cleaned and activated with air plasma (0.8 mbar with a power of 50 W for 60 s) and stored in PBS until used. PolyHIPEs were later sterilised by submerging them in 70% ethanol for 3 h under agitation, followed by three PBS washes. From each group, sterile polyHIPEs ($n = 45$) were assigned using an online random number generator (RNG) in groups of nine across five 24-well plates. The scaffolds were then immersed in cell culture media for 1 h. Afterwards, Y201 BMSCs cells, passage 79, were seeded dropwise onto scaffolds at a seeding density of 6×10^4 cells in 50 µl of basal medium. Samples were placed in a humidified incubator at 37 °C, 5% CO₂, for cell attachment. After 1 h, 450 µl of basal medium was added to each well, and after 24 h, scaffolds were transferred to a new plate. Each plate was assigned by RNG to be cultured for 7, 14, or 21 days in basal media or for 21 days in osteogenic media. For scaffolds allocated to osteogenic conditions (two plates,

$n = 18$), osteogenic supplements were added on day 3, consisting of 100 nM dexamethasone (D1756, Sigma), 50 µg ml⁻¹ L-ascorbic acid 2-phosphate sesquimagnesium salt hydrate (A8960, Sigma), and 5 mM β-glycerophosphate disodium salt hydrate (G9422, Sigma). All cells were cultured in a humidified incubator at 37 °C with 5% CO₂, and media was replenished every 7 days. Positive controls were cells grown on tissue culture polystyrene (TCP) (7600 cells per well) [25]. Acellular scaffolds were used as negative controls and blanks, helping to account for any background signal from the scaffold material itself. Controls were cultured under the same conditions as the samples. Before experiments, resazurin, DNA quantification, alkaline phosphatase (ALP), SR (Sirius red or direct red), AR (alizarin red), and fluorescence staining assays were pre-undertaken on Y201 BMSCs cultured on TCP to validate the assays. ALP was measured up to day 21, as prior research indicated that its levels in Y201 cells are either low or undetectable before this time [25, 26].

2.7. Resazurin reduction assay

The cell metabolic activity of Y201 BMSCs on the scaffolds was measured with a resazurin assay. Although resazurin is considered non-toxic, previous observations showed it can cause cell detachment after repeated assays over time [27]. Therefore, assays were carried out in different scaffolds at 20 h ($n = 3$, per group), 7, 14, or 21 days of culture ($n = 9$ per group). Briefly, a 1 mM stock solution of resazurin sodium salt (R7017, Sigma) was prepared, filtered (0.2 µm pore diameter, Fisher), and stored at 4 °C until used. A resazurin working solution (10% v/v) was prepared in PBS on the same day of use [27]. After removing the media from the samples, 500 µl of the resazurin working solution was added to each sample and incubated in the dark for 2 h in a humidified incubator at 37 °C and 5% CO₂. Afterwards, 150 µl from each sample was transferred per triplicate into a 96-well plate and read using a microplate reader (Tecan infinite 200-pro), using an excitation wavelength of 540 nm and an emission wavelength of 590 nm. Immediately following resazurin measurement, scaffolds were rinsed three times with PBS and fixed with 3.7% (w/v) formaldehyde (PFA) (252549, 35%, Sigma-Aldrich) for 40 min at RT. Scaffolds ($n = 3$ per group) were assigned using an online RNG for fluorescence staining, histological analysis, and confocal microscopy.

2.8. Fluorescence staining

PFA-fixed scaffolds ($n = 3$ per group) from day 7 were washed in PBS, permeabilised for 5 min with 0.1% v/v Triton X-100 (T8787, Sigma) made in PBS, blocked for 15 min with 1% w/v bovine serum albumin (A2153, LOT# SLBZ6632, Sigma) made in PBS, stained at RT in the dark for 40 min with 100 nM Acti-stain 488 Pallodin solution (PHDG1, LOT# 033,

Cytoskeleton, Inc.) in PBS, and counterstained for 1 min with a 1:1000 of 10 mg ml⁻¹ of 6-diamidino-2-phenylindole (DAPI, 32 670, Sigma-Aldrich) solution in PBS. Scaffolds were rinsed with PBS, mounted on a microscope slide, and observed under a fluorescent microscope (Olympus, IX73) at 10X. Using Image J, cell and nuclear aspect ratios were measured in 50 cells from images of scaffolds. Cell aspect ratio (CAR) is defined as the major axis divided by the minor axis, while nuclear aspect ratio (NAR) is defined as width divided by length.

2.9. Histological analysis

PFA-fixed scaffolds ($n = 3$ per group) from day 21 were cut in half with a scalpel and placed in plastic histology cassettes (M493-Histosette). Sequential dehydration in industrial methylated spirit (IMS) (99%, Fisher) (70%, 70% 80%, 85%, 90%, 95%, 100%, 100%), clarification in xylene (97%, Fisher), and paraffin wax infiltration were performed using a tissue processor (Leica, TP1020) for 18 h. Subsequently, each half of the scaffold was placed vertically in a wax box, dispensed with melted paraffin, and solidified on a cold plate (-10°C) in an embedding workstation (HistoStar, EpreDia). Sections of 5 μm were cut from the paraffin wax blocks with a microtome (Leica, RM2145). These were transferred to a paraffin section mounting bath (40°C) to flatten them, mounted on a Superfrost adhesion microscope slide, and dried at 37°C for 48 h. Slides were deparaffinised with xylene twice for 5 min and transferred twice to 100% ethanol for 2 min. The slides were rehydrated with 90% IMS and dH₂O for 2 min each. The sections were stained with haematoxylin (105175, Merck) for 25 s, cleared in tap water, and rehydrated in 70% and 90% ethanol for 2 min each. The slides were then stained with eosin (117081, Merck) for 30 s and further dehydrated for 30 s in 100% ethanol. The slides were placed in xylene for 1 min and then for 5 min before mounting with DPX (D/5319, Thermo Fisher Scientific). Once DPX dried, pictures of the slides under a light microscope (Olympus CX43) at 4X were taken.

2.10. Confocal microscopy

PFA-fixed scaffolds ($n = 3$ per group) from day 21 were stained with 100 nM Acti-stain 488 Pallodin for 1.5 h at RT. Imaging was performed at 10X on a confocal microscope (Leica SP8 TCS) equipped with a 488 nm Argon laser. Confocal z -sections were made throughout the bottom and top of scaffolds using 4.2 μm steps, or approximately 97 steps, with an image format of 512×512 . Around 97–93 images were stacked together to render a 3D image using the tools of LASX software.

2.11. DNA quantification and ALP measurement

After 21 d of cell culture with osteogenic supplements, scaffolds ($n = 9$ per group) were washed twice

with PBS and then lysate overnight at -80°C in a 10% v/v lysis buffer; 1 M tris-solution (SC-296 649, Chem Cruz), 1 mM ZnCl₂ (208086, Sigma), 1 mM MgCl₂ (M8266, Sigma) prepared with dH₂O with 1% v/v Triton-X100 [28]. Subsequently, scaffolds were exposed to three freeze-thaw cycles (-80°C to 37°C), vortexed, and centrifuged for 5 min at 10 000 rpm. A 1:200 working solution was prepared by diluting the Quant-iT reagent in a Quant-iT buffer from a Quant-iT[®] dsDNA assay kit (Q33120, Invitrogen). Then, 10 μl of the cell lysate in triplicate and 90 μl of the working solution were added into a black 96-well plate, shaken for 10 s in a microplate reader, and incubated for 10 min to allow the DNA to conjugate with the reagent. Fluorescence was measured at an excitation wavelength of 485 nm and an emission wavelength of 535 nm. Samples were processed in three batches, and measured fluorescence was converted to ng of DNA using individual standard curves made with DNA standards. Following DNA quantification, ALP activity from the same samples was measured. ALP substrate solution was prepared by dissolving in 5 ml of 20% v/v diethanolamine buffer (34066, 5X, Thermo Fisher Scientific) diluted in dH₂O, a tablet of p-nitrophenol phosphate (34047, Thermo Fisher Scientific). 10 μl of the cell lysate in triplicate and 90 μl of the ALP substrate solution were mixed in a 96-well plate. The plate was left at RT for around 15 min or until a yellowish colour appeared. Absorbance at 405 nm was read every min for 30 min with a microplate reader (Tecan Infinite 200-Pro). ALP activity was indicated as nmol p-nitrophenol min⁻¹ (nmolPNP min⁻¹), where one absorbance value is 19.75 nmol of product, then normalised to total DNA [29].

2.12. Alizarin red and direct red staining

Scaffolds ($n = 9$ per group) from cell culture in osteogenic supplements were fixed in 3.7% (w/v) PFA for 40 min at RT, rinsed with dH₂O, and submerged in 1% w/v AR (pH = 4.1) (A5533, Sigma-Aldrich) for 30 min on an orbital shaker (150 rpm) at RT. AR excess was removed by washing with dH₂O under orbital agitation. Then, 500 μl of 5% perchloric acid (311413, 60%, Sigma) was added for 15 min to destain the samples. 150 μl from each sample was transferred in triplicate to a 96-well plate and read in a microplate reader at 405 nm [29]. After destaining, scaffolds were washed five times every 30 min with dH₂O.

1% w/v of Direct Red 80 (365548, 25%, Sigma) was prepared with picric acid (P6744, 1.3%, Sigma) and filtered (0.2 μm pore diameter, Fisher Scientific). For AR destaining, scaffolds were submerged in the solution for 18 h under orbital shaking (150 rpm), and the excess was removed by washing with dH₂O every 5 min. Scaffolds were de-stained for 20 min with a solution of 0.2 M NaOH:methanol (1:1) [30]. 150 μl

from each sample was transferred in triplicate to a 96-well plate and read using a microplate reader at an absorbance of 540 nm.

2.13. Statistical analysis

Results from polyHIPEs characterisation and FITC-dextran were averaged and presented as mean \pm standard deviation (SD). Subsamples (triplicates) of each sample were averaged and taken as one reading. Blank data was also subtracted from each reading. Descriptive and statistical analyses were performed using GraphPad Prism 10 software (UK). Outliers were identified using the ROUT method ($Q = 1$). Outliers were removed from pore-diameter results before plotting the histograms. No data points were excluded for resazurin, ALP/DNA, AR, SR, NAR, or CAR analyses. A normality test ($\alpha = 0.05$) was performed on the data (D'Agostino–Pearson). For data with a normal distribution, the differences between groups were determined by one-way or two-way analysis of variance (ANOVA), with a 95% confidence interval ($\alpha = 0.05$). Comparisons between groups were performed based on Tukey's multiple comparisons. Otherwise, the data was compared with a Kruskal–Wallis test and Dunn's multiple comparisons.

3. Results and discussion

3.1. Increased internal phase fraction on PolyHIPE structure

SEM observations of polyHIPEs' cross-sections showed spherical porous interconnected structures (figure 2(A)). The porosity of the polyHIPEs correlated with their internal phase fraction (table 1). Key structural parameters, including pore diameter, DOO, and the frequency and size of pore interconnects, were measured to characterise their porous structure further. The pore size ranged from 20 to 200 μm (figure 2(B)), with median values of 70.4, 76.1, and 76.3 μm for P75, P80, and P85, respectively. Increasing the internal phase fraction from 75%–85% v/v did not significantly affect the pore diameters. Since our study investigated the effect of scaffold interconnectivity on BMSCs behaviour, maintaining the pore size range across the polyHIPEs was fundamental. SEM images confirmed that pore interconnects were well-defined and spherical (figure 2(A)), implying they formed during the emulsification process rather than post-washing steps [9]. The size and frequency of interconnects per pore, along with the DOO, increased with the internal phase volume (table 1). These findings align with previous observations observed with mercury intrusion porosimeter, which similarly showed an increase in both the number and diameter of pore interconnects with increasing internal phase [10]. This effect arose because, while the number of particles used was sufficient to stabilise 75 H, a slight increase in the internal phase

volume created instabilities that enhanced interconnectivity within the polyHIPEs. This trend is consistent with findings from Owen *et al*, reporting a steady rise in DOO as the internal phase volume increased from 75%–85% v/v [31]. Similarly, Mert *et al* noted that the internal phase fraction is a dominant factor in determining interconnect pore sizes, with larger sizes as the internal phase volume increases [32]. This aspect of pore morphology is particularly relevant when considering the Euler number, a valuable topological descriptor for characterising the connectivity of porous structures. A lower Euler number signifies a greater number of holes and interconnections within the pore network, thus indicating enhanced pore connectivity [33]. The Euler number (E) is calculated using the following relationship, where β_o is the number of pores, β_1 is the number of connections in the pore space, and β_2 is the number of closed cavities/pores [11].

$$E = \beta_o - \beta_1 + \beta_2 \quad (4)$$

3D micro-CT analysis revealed an inverse relationship between the Euler number and the DOO of the polyHIPEs (table 1). This observation aligns with existing knowledge that the Euler number is influenced by porosity, pore diameter and pore geometry [33]. These findings collectively demonstrate that size and number of pore interconnects/throats significantly impact the overall pore interconnectivity.

3.2. Attachment and proliferation were similar across the polyHIPEs

Y201 cell attachment was found to be similar on the three scaffolds, as determined by a resazurin assay ($n = 3$ per group) (figure 3(A)). Cells were observed to be distributed across the scaffold surfaces (figure 3(B)). The maximum cell infiltration depth cells recorded from confocal images ($n = 3$ per group) were $103 \pm 22 \mu\text{m}$ for P75, $138 \pm 19 \mu\text{m}$ for P80 and $189 \pm 45 \mu\text{m}$ for P85. The increased porosity and interconnectivity in P85 likely facilitated the deeper infiltration of cells into the scaffold structure. It is well-established that structural properties of scaffolds significantly influence cell seeding efficiency, often leading to cell trapping and aggregation on the scaffold's surface [34] or low attachment due to large pores, or sedimentation at the scaffold base due to cells falling through large interconnects [35]. Therefore, the cell distribution of the scaffolds after seeding can be directly attributed to variation in pore characteristics. Static seeding can sometimes lead to cell sedimentation at the bottom of scaffolds, but no cells were detected at the scaffold base. However, a significant number of cells adhered to some regions of the scaffolds' periphery, extending to the base side (figure 3(C)). This peripheral attachment subsequently accounts for the presence of some

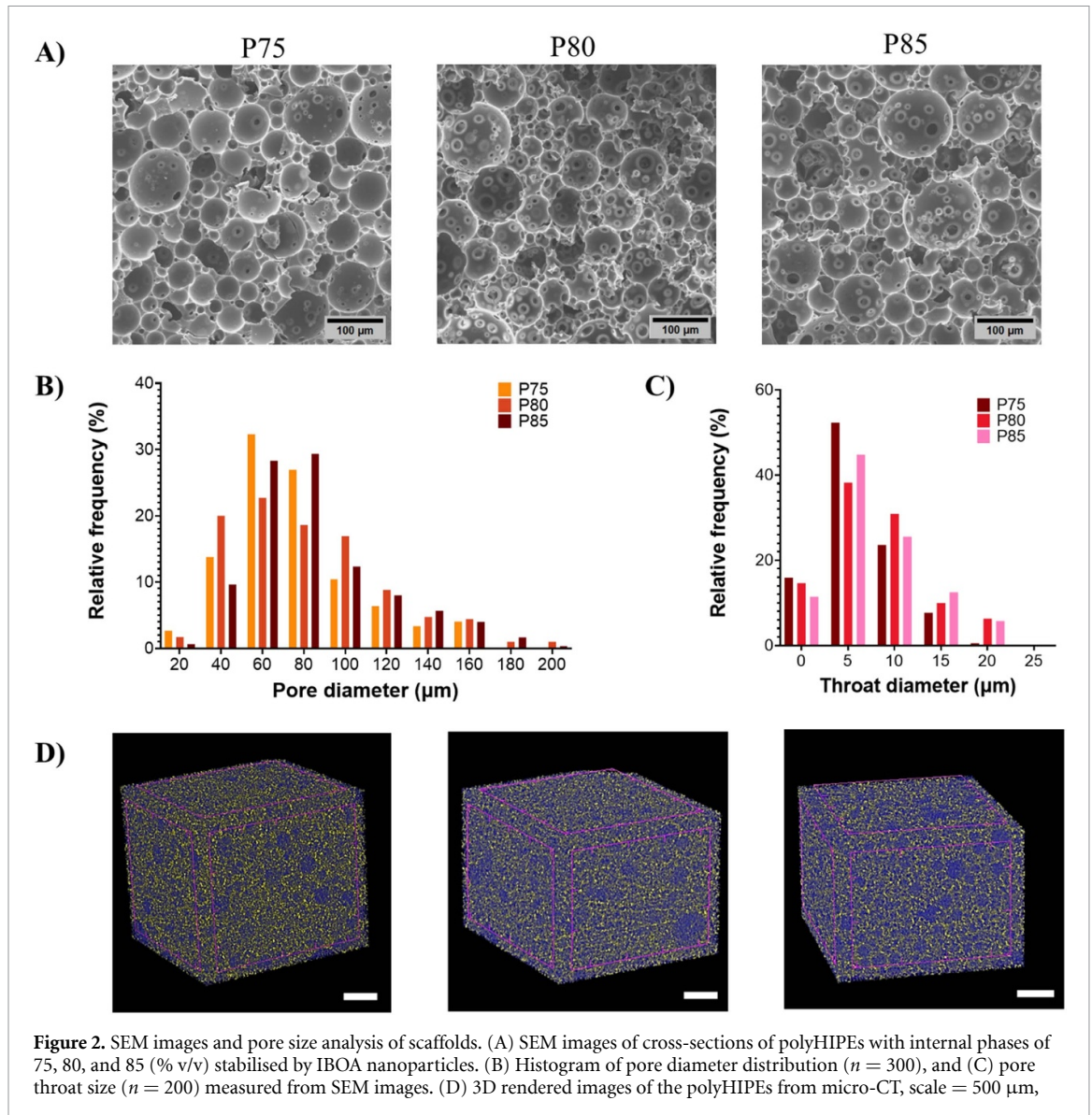


Figure 2. SEM images and pore size analysis of scaffolds. (A) SEM images of cross-sections of polyHIPEs with internal phases of 75, 80, and 85 (% v/v) stabilised by IBOA nanoparticles. (B) Histogram of pore diameter distribution ($n = 300$), and (C) pore throat size ($n = 200$) measured from SEM images. (D) 3D rendered images of the polyHIPEs from micro-CT, scale = 500 μm ,

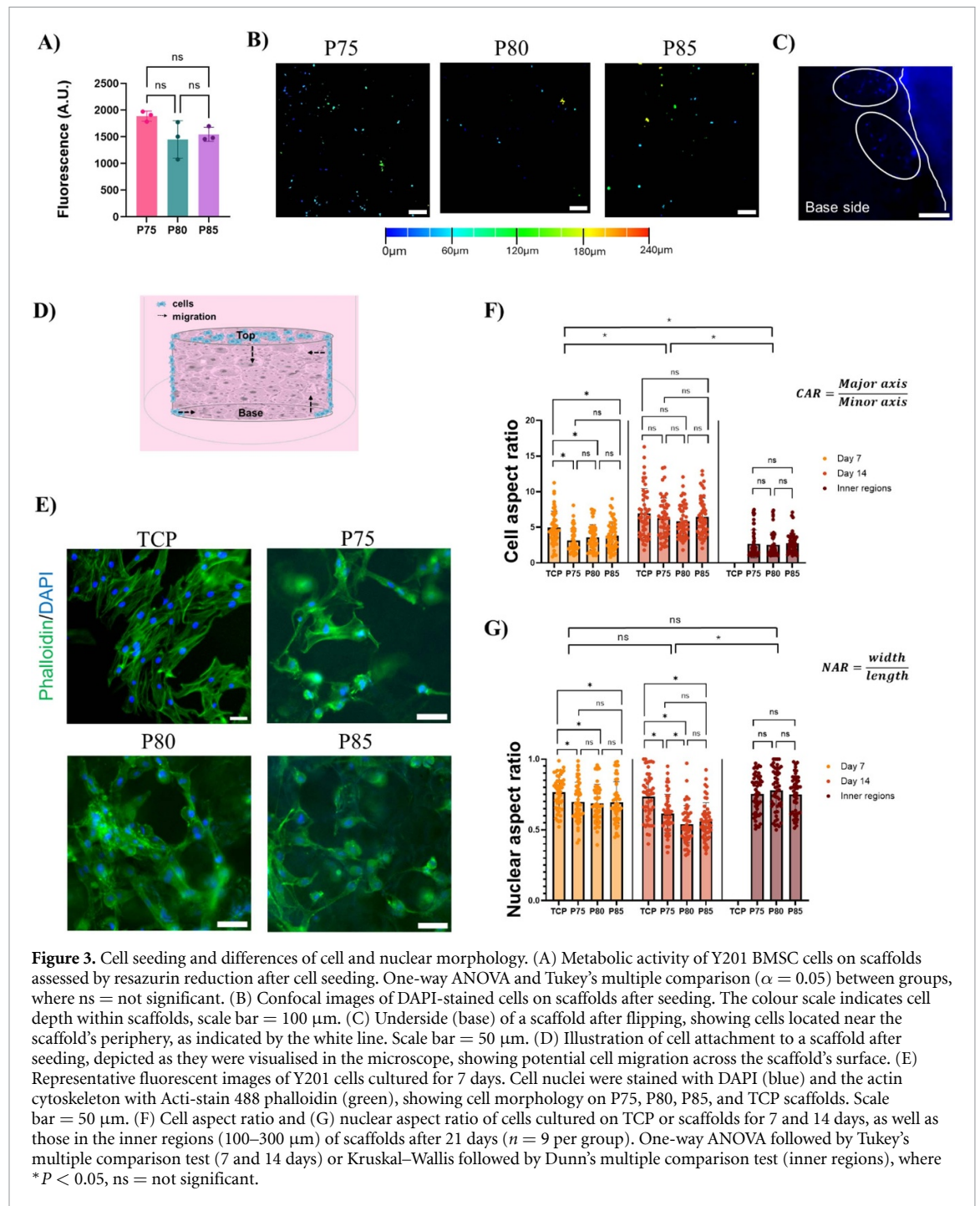
Table 1. Median of pore diameter (D_p), and interconnects diameter (D_{pt}), mean \pm SD of interconnects per pore (N_t), degree of openness (DOO), density (ρ), % porosity (P) of polyHIPEs measured from SEM. Euler # obtained from micro-CT.

Internal phase (% v/v)	D_p (μm)	D_{pt} (μm)	N_t	DOO	ρ (g cm^{-3})	P (%)	Euler #
75	70.4	4.84	6 \pm 4	0.031 \pm 0.01	0.18 \pm 0.03	72.8 \pm 2.4	-600 389
80	76.1	6.95	10 \pm 8	0.086 \pm 0.06	0.13 \pm 0.01	80.5 \pm 3.8	-18 462 291
85	76.3	6.92	20 \pm 14	0.129 \pm 0.06	0.11 \pm 0.01	84.0 \pm 4.2	-24 287 626

cells on the bottom of the scaffolds (figure 7). It is hypothesised that these cells migrated from the periphery to the scaffolds bottom surface over time, and then towards the innermost part of the scaffolds, as documented previously [35] (figure 3(D)).

Y021 cells attached and oriented around the pores, preferably the large ones (figure 3(E)). Cells positioned at the pore's struts, where they migrated in multiple directions along or towards more struts to form a 'bridge' morphology, as shown in other studies [36]. Cell morphology was assessed using the CAR and NAR and compared to cells cultured on a flat substrate, TCP. At day 7, Y201 BMSCs on TCP

exhibited a more spread morphology with a median CAR of 4.53. In comparison, cells seeded on scaffolds showed higher values, 2.66, 3.35, and 3.57 for P75, P80, and P85, respectively, with no significant differences between the scaffold groups (figure 3(F)). This initial difference is likely due to the scaffolds' curved surface, which causes cells to adopt their shape to the curvature [37]. As cells proliferate and spread to cover more of the surface, they become more elongated (6.3 for TCP, 6.2 for P75, 5.3 for P80 and 6.0 for P85). By day 14, the cell morphology on the scaffolds has become more like that on the TCP surface. The high aspect ratio observed in these cells is associated with



cellular migration and spreading as they interact with the surface of the scaffold and neighbouring cells [38].

At day 7, the NAR, where values close to 1 indicate a more spherical structure and <1 a more elongated shape, medians were slightly lower for scaffolds, with values of 0.68, 0.66, and 0.67 for P75, P80, and P85, respectively, compared to 0.79 for TCP (figure 3(G)). The slightly lower values on scaffolds were likely due to confined spaces. Cell migration through constricted spaces, such as pores, is limited by the nucleus, also noted in other studies involving MSC migration in constrained spaces [39, 40]. By day 14, this

nuclear compression was more pronounced in scaffolds. Interestingly, cells found in inner regions of the scaffolds exhibited a reduction in the cellular aspect ratio and, in consequence, a less compress nucleus, as cells are moving to new areas, they adapt their shapes to the available surface area [37]. While the nucleus can often recover from wrinkles made after passing through tight constrictions [41], further research is required to determine whether this process leads to DNA damage in our specific study.

In general, the porous architecture of scaffolds supports cell adhesion and proliferation. Actin fibres

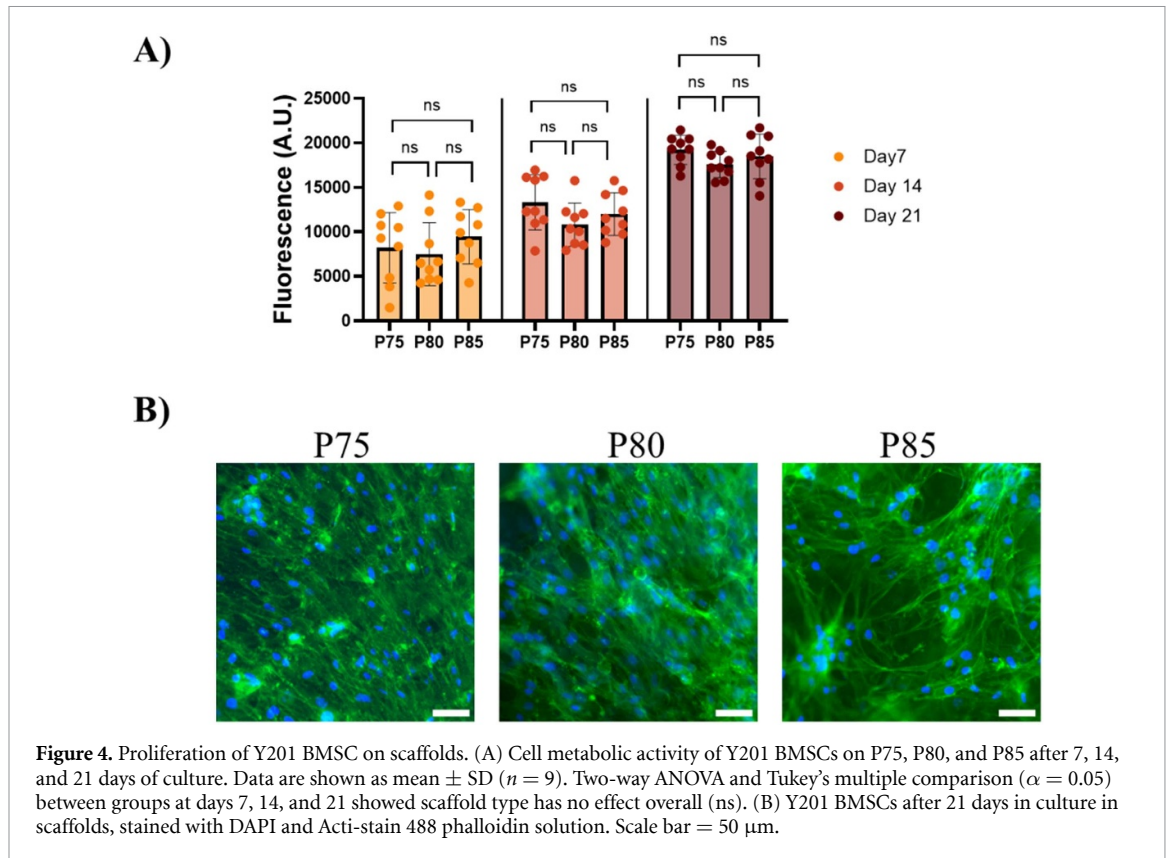


Figure 4. Proliferation of Y201 BMSC on scaffolds. (A) Cell metabolic activity of Y201 BMSCs on P75, P80, and P85 after 7, 14, and 21 days of culture. Data are shown as mean \pm SD ($n = 9$). Two-way ANOVA and Tukey's multiple comparison ($\alpha = 0.05$) between groups at days 7, 14, and 21 showed scaffold type has no effect overall (ns). (B) Y201 BMSCs after 21 days in culture in scaffolds, stained with DAPI and Acti-stain 488 phalloidin solution. Scale bar = 50 μ m.

and nuclei staining after 21 days in culture confirmed that cells proliferated, extending across pores and eventually closing them (figure 4(B)). However, no significant differences between the scaffolds by days of culture (figure 4(A)) were observed by the resazurin reduction assay.

3.3. Pore interconnectivity enhanced dextran diffusion and Y201 BMSCs migration on the polyHIPEs

In this study, nutrient transport within the scaffolds occurred solely via diffusion due to static cell culture conditions. To assess diffusion within scaffolds, they were immersed in a FITC-dextran solution. To eliminate autofluorescence from scaffolds or petri dishes, scaffolds were previously stained with Sudan black (figure 5(A)). Confocal images were taken after 15 min. The diffusivity was inferred from the fluorescence intensity measured at the centre of the poly-HIPEs. P85 exhibited the highest dextran diffusion, as demonstrated by significantly elevated fluorescence intensity compared to P75 and P80 (figure 5(B)). Specifically, the relative fluorescence intensities were 5.9 ± 2.2 , 8.1 ± 3.6 , and 27 ± 4.2 for P75, P80, and P85, respectively. The increased diffusion observed in P85 can be attributed to enhanced porosity and interconnectivity, as the pore diameter range was maintained constant across the scaffolds. The diffusion of FITC-dextran was measured under static conditions, aligning with the experimental setup.

While not assessed in this study, FITC-dextran flow could also be measured dynamically, for instance, by incorporating scaffolds into microfluidic devices [42]. This would enable observation of the relationship between interconnectivity and permeability.

The migration of Y201 BMSCs into the scaffolds was observed by haematoxylin & eosin staining and confocal imaging after 21 days of culture. Staining (figure 6) depicted that Y201 BMSCs initially lined the outer surface of the scaffolds, forming a dense cell layer. Over time, cells migrated from the scaffold's edges (top and bottom) towards the centre. Visually, among the scaffolds, P85 showed the most extensive cell infiltration, with more cells distributed throughout the scaffold cross-section. Confocal images further validated these findings, illustrating cell density and migration (figure 7). Cell migration was defined as the depth at which the cells in the scaffolds were found, considering the first cells found on the scaffold surface. The migration depths from the top of the scaffold were 268 ± 81 μ m for P75, 280 ± 52 μ m for P80, and 348 ± 27 μ m for P85. From the bottom of the scaffold, the corresponding migration depths were 245 ± 35 μ m, 219 ± 50 μ m, and 340 ± 31 μ m, respectively. The P85 scaffolds exhibited the greatest migration depth, while P75 and P80 were comparable. Notably, this migration trend correlated with FITC-dextran diffusion results. Overall, studies emphasise the role of pore interconnectivity in scaffolds for efficient cell infiltration. Larger

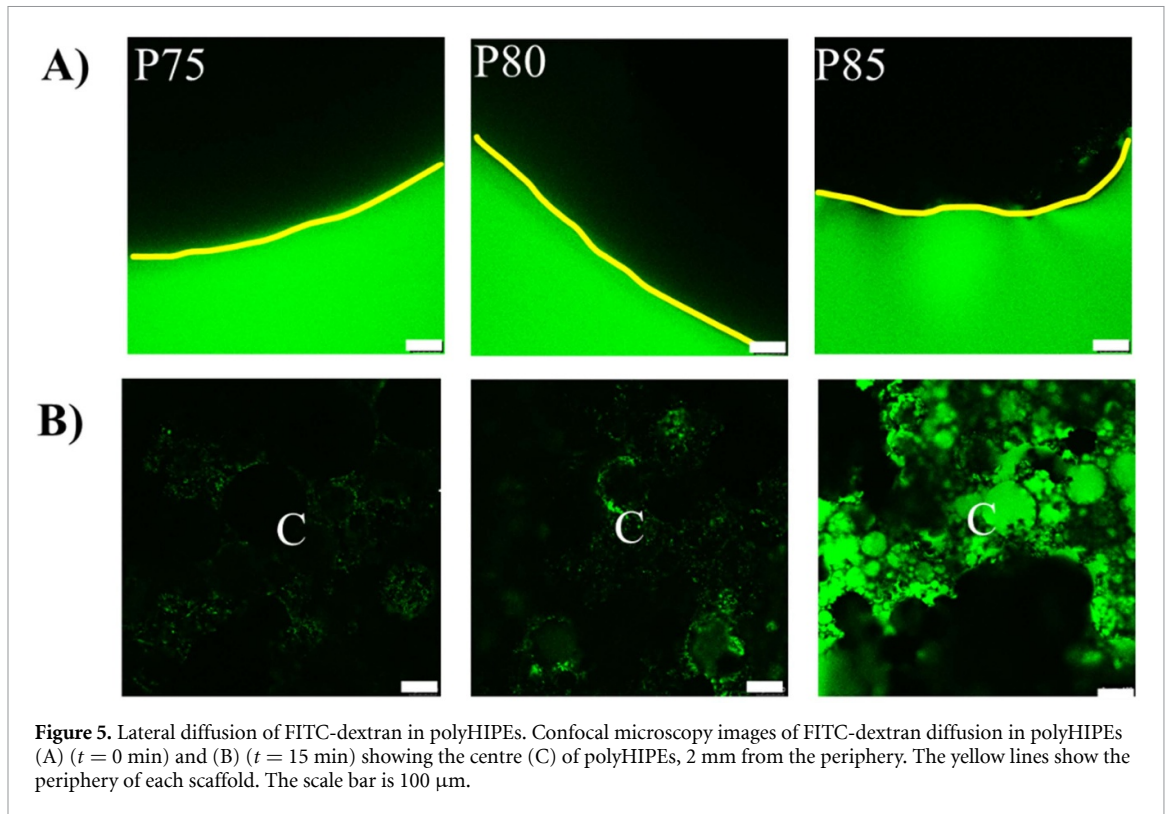


Figure 5. Lateral diffusion of FITC-dextran in polyHIPEs. Confocal microscopy images of FITC-dextran diffusion in polyHIPEs (A) ($t = 0$ min) and (B) ($t = 15$ min) showing the centre (C) of polyHIPEs, 2 mm from the periphery. The yellow lines show the periphery of each scaffold. The scale bar is 100 μm .

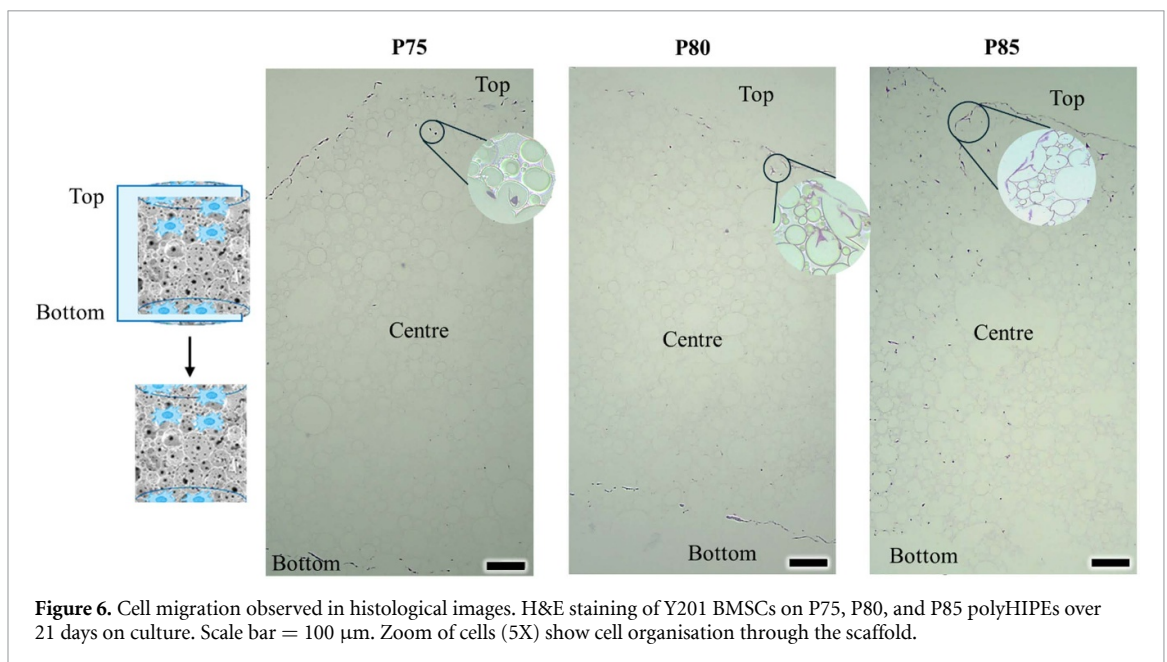
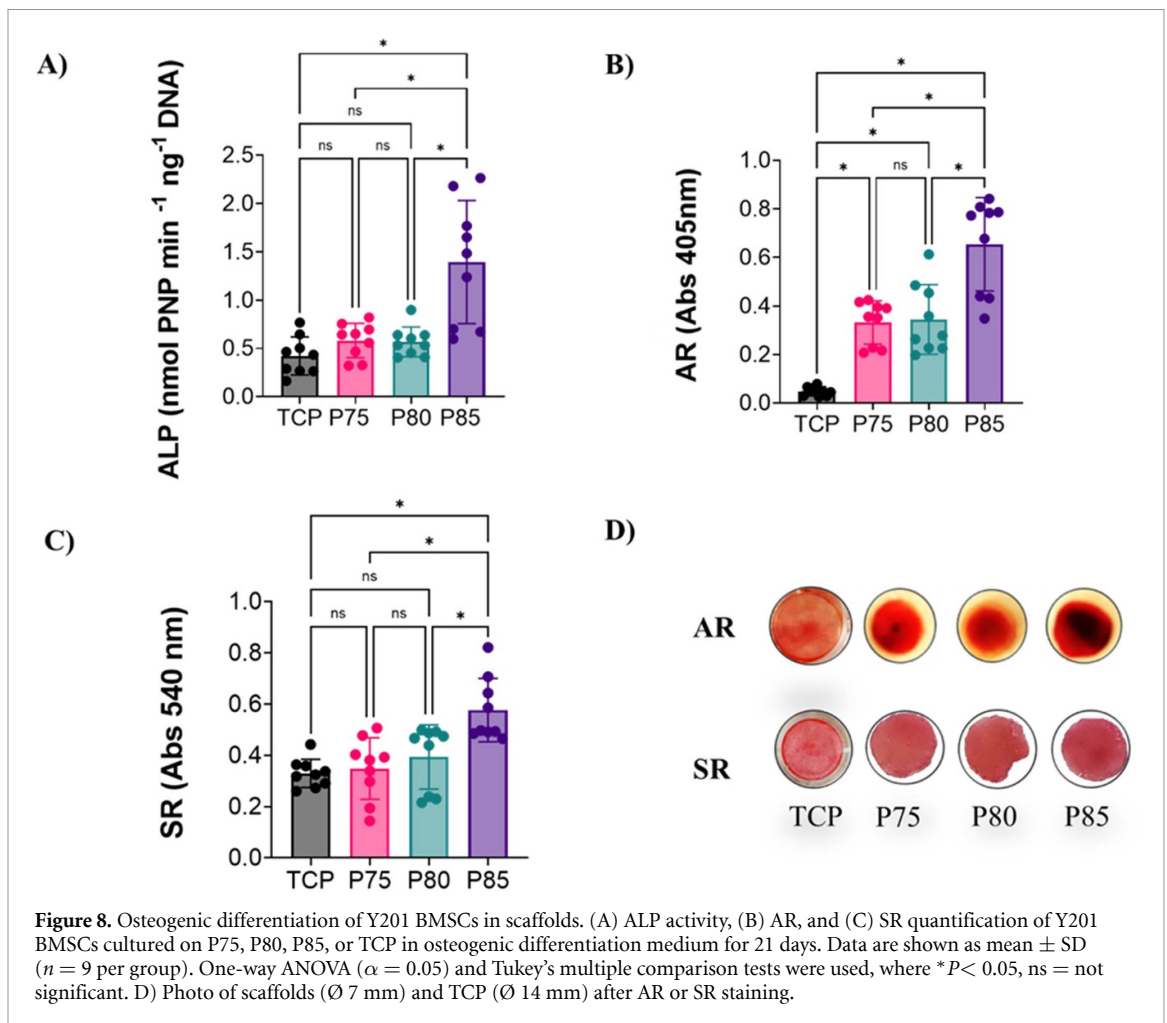
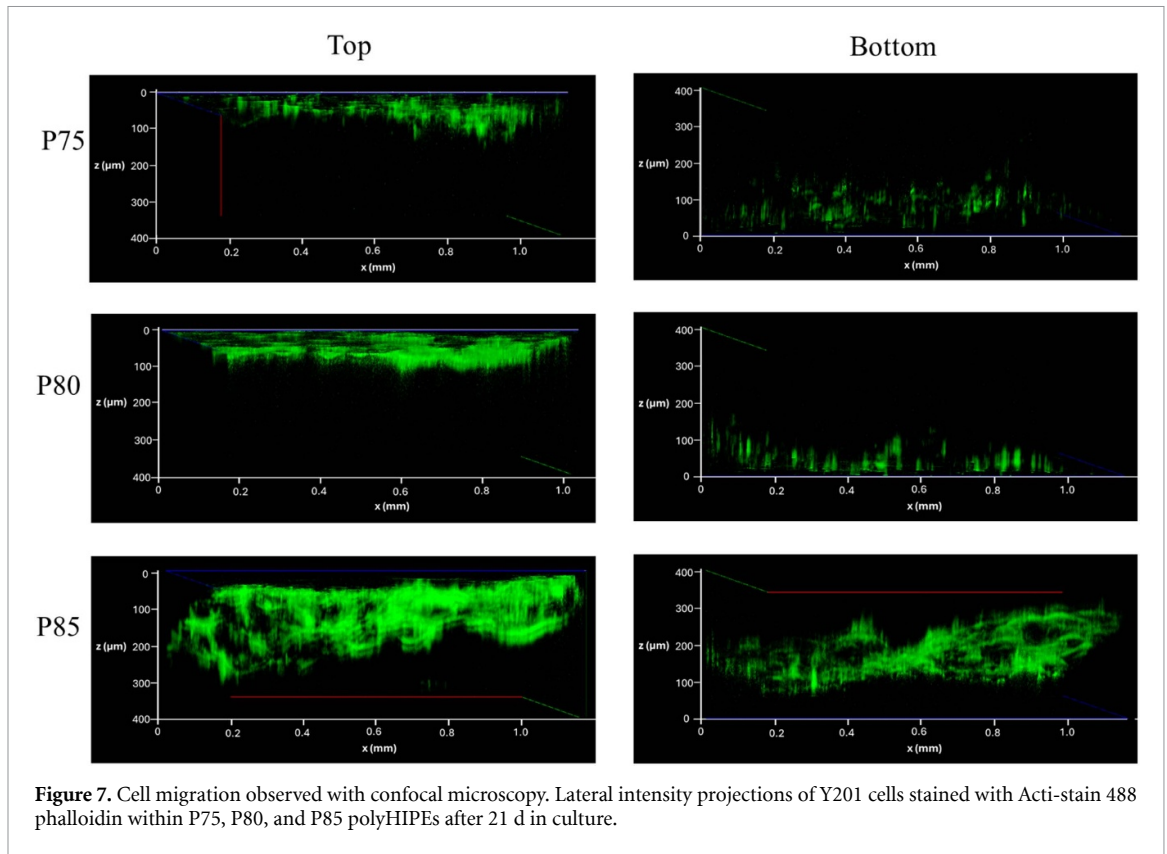


Figure 6. Cell migration observed in histological images. H&E staining of Y201 BMSCs on P75, P80, and P85 polyHIPEs over 21 days on culture. Scale bar = 100 μm . Zoom of cells (5X) show cell organisation through the scaffold.

pore interconnects are associated with improved cell migration [43] and permeability. For example, Jia *et al* [35] demonstrated that increased pore interconnect size enhanced cell movement and scaffold permeability. Similarly, Lu *et al* reported that interconnected channels promote greater cell migration in ceramic scaffolds [44]. Together, these data indicate that a high pore interconnectivity was essential for promoting nutrient transport and BMSCs migration.

3.4. PolyHIPE interconnectivity promoted the osteogenic differentiation of Y201 BMSCs

The early osteogenic differentiation of Y201 BMSCs was evaluated after 21 days of culture by assessing ALP activity and calcium and collagen deposition. ALP activity normalised to DNA content (figure 8(A)) revealed that P85 had the highest ALP activity compared to P75 and P80. Specifically, the mean values were 0.59 ± 0.16 for P75, 0.60 ± 0.16 for P80, 1.39 ± 0.6 for P85, and



0.35 ± 0.11 nmol PNP min^{-1} ng^{-1} DNA for TCP. Additionally, extracellular calcium secretion and collagen production mirrored the ALP results, with P85 showing the highest calcium and collagen production. Quantitative results showed collagen production on P85 was approximately 1.8 times higher than for P75 or P80 (figure 8(C)). Similarly, calcium deposition and ALP activity in P85 were 1.9 and 2.35 times higher than in P75 and P80 (figure 8(B)).

Numerous studies emphasise the role of porous scaffold structures in enhancing the osteogenic differentiation of MSCs. For instance, Phadke *et al* [45] and Fu *et al* [46] compared scaffolds with two architectures, one porous and one more columnar, finding that a more porous scaffold led to greater MSC osteogenic differentiation. About the pore size, studies have shown that porous scaffolds with pore sizes larger than 400 μm [47], around 300–100 μm [48] promoted the osteogenic differentiation of human MSCs. However, pore interconnectivity contributes to cell infiltration, promoting a 3D cell distribution that supports cell-cell and cell-matrix interactions relevant to osteogenic signalling and differentiation pathways [49, 50]. Studies have shown that such spreading and uniform distribution of cells within scaffolds increases osteogenic differentiation [51, 52]. Lo *et al* further demonstrated that pore geometry and spatial constraints within scaffolds affect cytoskeleton organisation, impacting MSC differentiation [53]. Therefore, the observed increase in osteogenic differentiation on P85 scaffolds can be attributed to its higher pore interconnectivity, facilitating cell ingrowth, homogeneous distribution, and cell signalling necessary for effective osteogenic responses.

4. Conclusions

This study synthesised porous scaffolds with a consistent pore size range but varied interconnectivity, enhancing the tunability of scaffold characteristics crucial for BTE. By increasing the internal phase fraction from 75% to 85%, the scaffolds exhibited a greater DOO along with a higher number and size of pore interconnects per pore, resulting in more effective nutrient diffusion, as observed through FITC-dextran diffusion tests under static conditions. Human BMSCs seeded onto these polyHIEPs demonstrated successful attachment and continuous proliferation over time. The results emphasise that higher pore interconnectivity promotes better cell infiltration and facilitates cell-cell and cell-extracellular matrix interactions, which could enhance osteogenic differentiation. Therefore, optimising pore interconnectivity is an important factor in scaffold design for BTE, as it directly influences cell behaviour and supports effective bone regeneration. Our novel method allows selective tuning of this critical property. While this study investigated the effect of pore interconnectivity on MSC migration and infiltration, future

research could explore the use of dynamic cell seeding and cell culture. This would provide valuable insights into cell distribution and migration under flow conditions.

Data availability statement

All data that support the findings of this study are included within the article (and any supplementary files).

Acknowledgments

AM-O acknowledges the scholarship with number 795349 granted by the National Council of Science and Technology (CONACYT, now SECIHTI). Authors thank Professor Paul Genever (University of York) for supplying the BMSC clonal line Y201.

Ethical statement

Ethical approval was not required for this work because the Y201 human bone marrow stromal cell line was provided by Professor Paul Genever of the University of York under a Material Transfer Agreement. The cell line's original derivation received ethical approval from the National Research Ethics Service and the University of Manchester, as previously documented (doi: [10.1016/j.stemcr.2015.05.005](https://doi.org/10.1016/j.stemcr.2015.05.005)).

ORCID iDs

Areli Munive-Olarte  0000-0002-8612-5001

Enes Durgut  0000-0002-2224-7325

Stefaan W Verbruggen  0000-0002-2321-1367

Frederik Claeysens  0000-0002-1030-939X

Gwendolen C Reilly  0000-0003-1456-1071

References

- [1] Zhang Y *et al* 2020 Stem cell-friendly scaffold biomaterials: applications for bone tissue engineering and regenerative medicine *Front. Bioeng. Biotechnol.* **8** 598607
- [2] Mukasheva F, Adilova L, Dyussenbinov A, Yernaimanova B, Abilev M and Akilbekova D 2024 Optimizing scaffold pore size for tissue engineering: insights across various tissue types *Front. Bioeng. Biotechnol.* **12** 1444986
- [3] Abbasi N, Hamlet S, Love R M and Nguyen N T 2020 Porous scaffolds for bone regeneration *J. Sci.* **5** 1–9
- [4] Salehabadi M and Mirzadeh H 2025 3D printing of polyester scaffolds for bone tissue engineering: advancements and challenges *Adv. Mater. Technol.* **10** 2401522
- [5] Gavazzo P, Viti F, Donnelly H, Oliva M A G, Salmeron-Sanchez M, Dalby M J and Vassalli M 2021 Biophysical phenotyping of mesenchymal stem cells along the osteogenic differentiation pathway *Cell Biol. Toxicol.* **37** 915–33
- [6] Jiao J, Hong Q, Zhang D, Wang M, Tang H, Yang J, Qu X and Yue B 2023 Influence of porosity on osteogenesis, bone growth and osteointegration in trabecular tantalum scaffolds fabricated by additive manufacturing *Front. Bioeng. Biotechnol.* **11** 1117954

- [7] Deng F, Liu L, Li Z and Liu J 2021 3D printed Ti6Al4V bone scaffolds with different pore structure effects on bone ingrowth *J. Biol. Eng.* **15** 4
- [8] Armatas G S 2006 Determination of the effects of the pore size distribution and pore connectivity distribution on the pore tortuosity and diffusive transport in model porous networks *Chem. Eng. Sci.* **61** 4662–75
- [9] Aldemir Dikici B and Claeysens F 2020 Basic principles of emulsion templating and its use as an emerging manufacturing method of tissue engineering scaffolds *Front. Bioeng. Biotechnol.* **8** 875
- [10] Durgut E, Sherborne C, Aldemir Dikici B, Reilly G C and Claeysens F 2022 Preparation of interconnected pickering polymerized high internal phase emulsions by arrested coalescence *Langmuir* **38** 10953–62
- [11] Thomas A, Agarwal A K, Kashyap Y S, Kumar I P and Bera J 2024 Quantifying pore characteristics in polymer glass–ceramics composite scaffolds using micro-tomography *J. Mater. Res.* **39** 1258–72
- [12] Elakkiya K, Bargavi P and Balakumar S 2023 3D interconnected porous PMMA scaffold integrating with advanced nanostructured CaP-based biomaterials for rapid bone repair and regeneration *J. Mech. Behav. Biomed. Mater.* **147** 106106
- [13] Schiavi A, Gaido F, Gabrieli R, Alidoost D, Schwentenwein M, Mohammadi M, Tulyaganov D, Verné E and Baino F 2025 Permeability and tomography-based microstructural analysis of ultra-porous bioactive glass scaffolds *Mater. Lett.* **384** 138064
- [14] Munive-Olarte A, Hidalgo-Moyle J J, Velasquillo C, Juarez-Moreno K and Mota-Morales J D 2022 Boosting cell proliferation in three-dimensional polyacrylates/nanohydroxyapatite scaffolds synthesized by deep eutectic solvent-based emulsion templating *J. Colloid Interface Sci.* **607** 298–311
- [15] Freeman F, Browe D, Nulty J, Von Euw S, Grayson W and Kelly D 2019 Biofabrication of multiscale bone extracellular matrix scaffolds for bone tissue engineering *Eur. Cells Mater.* **38** 168–87
- [16] Nga N K, Hoai T T, Anh N T N, Kim S, Kim S, Kim H D and Huh K M 2025 Solvent casting-salt leaching synthesis, characterization, and biocompatibility of three-dimensional porous chitosan/nano-hydroxyapatite scaffolds for bone tissue engineering *Macromol. Res.* **33** 667–82
- [17] Nayaju T, Shrestha D, Kang K, Maharjan B and Park C H 2025 Reconstructed three-dimensional structure of gas-foamed polycaprolactone/cellulose nanofibrous scaffold for biomedical applications *Int. J. Biol. Macromol.* **285** 138253
- [18] Katrilaka C, Karipidou N, Petrou N, Manglaris C, Katrilakas G, Tzavellas A N, Pitou M, Tsiridis E E, Choli-Papadopoulou T and Aggeli A 2023 Freeze-drying process for the fabrication of collagen-based sponges as medical devices in biomedical engineering *Materials* **16** 4425
- [19] Tan J L T, Shimabukuro M, Tsuchiya A, Wijekoon W, Kishida R, Kawashita M and Ishikawa K 2025 Influence of porogens on architecture and osteogenesis of porous carbonate apatite artificial bones *Ceram. Int.* **51** 19963–72
- [20] Durgut E and Claeysens F 2025 Pickering polymerized high internal phase emulsions: fundamentals to advanced applications *Adv. Colloid Interface Sci.* **336** 103375
- [21] Wang Z, Gao T, Cui L, Wang Y, Zhang P and Chen X 2016 Improved cellular infiltration into 3D interconnected microchannel scaffolds formed by using melt-spun sacrificial microfibers *RSC Adv.* **6** 2131–4
- [22] Aldemir Dikici B, Dikici S, Reilly G C, MacNeil S and Claeysens F 2019 A novel bilayer polycaprolactone membrane for guided bone regeneration: combining electrospinning and emulsion templating *Materials* **12** 2643
- [23] Offeddu G S, Mohee L and Cameron R E 2020 Scale and structure dependent solute diffusivity within microporous tissue engineering scaffolds *J. Mater. Sci., Mater. Med.* **31** 46
- [24] James S *et al* 2015 Multiparameter analysis of human bone marrow stromal cells identifies distinct immunomodulatory and differentiation-competent subtypes *Stem Cell Rep.* **4** 1004–15
- [25] Oliveira Rodrigues J R 2022 *Development of Osteoinductive Coatings for Spinal Implants (Fusion Cages)* (The University of Sheffield)
- [26] Bellucci D, Scalzone A, Ferreira A M, Cannillo V and Gentile P 2022 Adhesive bioinspired coating for enhancing glass-ceramics scaffolds bioactivity *Materials* **15** 8080
- [27] Hann A J 2023 *Development and Assessment of in Vitro Models of Osteogenic Microstructures* (The University of Sheffield)
- [28] Bhaskar B, Owen R, Bahmaee H, Rao P S and Reilly G C 2018 Design and assessment of a dynamic perfusion bioreactor for large bone tissue engineering scaffolds *Appl. Biochem. Biotechnol.* **185** 555–63
- [29] Delaine-Smith R M, Hann A J, Green N H and Reilly G C 2021 Electrospun fiber alignment guides osteogenesis and matrix organization differentially in two different osteogenic cell types *Front. Bioeng. Biotechnol.* **9** 672959
- [30] Sittichokechaiwut A, Edwards J, Scutt A and Reilly G 2010 Short bouts of mechanical loading are as effective as dexamethasone at inducing matrix production by human bone marrow mesenchymal stem cell *Eur. Cell Mater.* **20** 45–57
- [31] Owen R, Sherborne C, Paterson T, Green N H, Reilly G C and Claeysens F 2016 Emulsion templated scaffolds with tunable mechanical properties for bone tissue engineering *J. Mech. Behav. Biomed. Mater.* **54** 159–72
- [32] Mert Hh, Mert Ms and Mert Eh. 2019 A statistical approach for tailoring the morphological and mechanical properties of polystyrene PolyHIPEs: looking through experimental design *Mater. Res. Express* **6** 115306
- [33] Mason P E, Darvell L I, Jones J M and Williams A 2016 Comparative study of the thermal conductivity of solid biomass fuels *Sustain. Energy Fuels* **30** 2158–63
- [34] Ali D 2019 Effect of scaffold architecture on cell seeding efficiency: a discrete phase model CFD analysis *Comput. Biol. Med.* **109** 62–69
- [35] Jia G *et al* 2021 Exploring the interconnectivity of biomimetic hierarchical porous Mg scaffolds for bone tissue engineering: effects of pore size distribution on mechanical properties, degradation behavior and cell migration ability *J. Magnes. Alloy* **9** 1954–66
- [36] Buenzli P R, Lanaro M, Wong C S, McLaughlin M P, Allenby M C, Woodruff M A and Simpson M J 2020 Cell proliferation and migration explain pore bridging dynamics in 3D printed scaffolds of different pore size *Acta Biomater.* **114** 285–95
- [37] Werner M, Blanquer S B G, Haimi S P, Korus G, Dunlop J W C, Duda G N, Grijpma D W and Petersen A 2017 Surface curvature differentially regulates stem cell migration and differentiation via altered attachment morphology and nuclear deformation *Adv. Sci.* **4** 1600347
- [38] Banik B L, Riley T R, Platt C J and Brown J L 2016 Human mesenchymal stem cell morphology and migration on microtextured titanium *Front. Bioeng. Biotechnol.* **4** 41
- [39] Doolin M T, Ornstein T S and Stroka K M 2019 Nuclear deformation in response to mechanical confinement is cell type dependent *Cells* **8** 427
- [40] Lu Q, Diao J, Wang Y, Feng J, Zeng F, Yang Y, Kuang Y, Zhao N and Wang Y 2023 3D printed pore morphology mediates bone marrow stem cell behaviors via RhoA/ROCK2 signaling pathway for accelerating bone regeneration *Bioact. Mater.* **26** 413–24
- [41] McKee B, Abolghasemzade S, Wang T C, Harsh K, Kaur S, Blanchard R, Menon K B, Mohajeri M, Dickinson R B and Lele T P 2025 Excess surface area of the nuclear lamina enables unhindered cell migration through constrictions *Sci. Adv.* **11** 1–13
- [42] Bahmaee H, Owen R, Boyle L, Perrault C M, Garcia-Granada A A, Reilly G C and Claeysens F 2020

- Design and evaluation of an osteogenesis-on-a-chip microfluidic device incorporating 3D cell culture *Front. Bioeng. Biotechnol.* **8** 557111
- [43] Singh Y P, Dasgupta S, Agrawal A K and Bhaskar R 2025 Quantitative analysis of reinforcement of nano-sized monetite particles on chitosan/gelatin 3D porous scaffolds using the micro-CT technique *J. Porous Mater.* **32** 1–14
- [44] Lu J X, Flautre B, Anselme K, Hardouin P, Gallur A, Descamps M and Thierry B 1999 Role of interconnections in porous bioceramics on bone recolonization *in vitro* and *in vivo* *J. Mater. Sci., Mater. Med.* **10** 111–20
- [45] Phadke A, Hwang Y, Hee Kim S, Hyun Kim S, Yamaguchi T, Masuda K and Varghese S 2013 Effect of scaffold microarchitecture on osteogenic differentiation of human mesenchymal stem cells *eCM* **25** 114–29
- [46] Fu Q, Rahaman M N, Bal B S and Brown R F 2009 Proliferation and function of MC3T3-E1 cells on freeze-cast hydroxyapatite scaffolds with oriented pore architectures *J. Mater. Sci., Mater. Med.* **20** 1159–65
- [47] Wang Y, Liu Y, Chen S, Francis Siu M F, Liu C, Bai J and Wang M 2025 Enhancing bone regeneration through 3D printed biphasic calcium phosphate scaffolds featuring graded pore sizes *Bioact. Mater.* **46** 21–36
- [48] Brennan C M, Eichholz K F and Hoey D A 2019 The effect of pore size within fibrous scaffolds fabricated using melt electrowriting on human bone marrow stem cell osteogenesis *Biomed. Mater.* **14** 065016
- [49] Yun C *et al* 2024 Advantages of using 3D spheroid culture systems in toxicological and pharmacological assessment for osteogenesis research *Int. J. Mol. Sci.* **25** 2512
- [50] Zauchner D, Müller M Z, Horrer M, Bissig L, Zhao F, Fisch P, Lee S S, Zenobi-Wong M, Müller R and Qin X-H 2024 Synthetic biodegradable microporous hydrogels for *in vitro* 3D culture of functional human bone cell networks *Nat. Commun.* **15** 5027
- [51] Melke J, Zhao F, Ito K and Hofmann S 2020 Orbital seeding of mesenchymal stromal cells increases osteogenic differentiation and bone-like tissue formation *J. Orthop. Res.* **38** 1228–37
- [52] Yang Y, Wang X, Wang Y, Hu X, Kawazoe N, Yang Y and Chen G 2019 Influence of cell spreading area on the osteogenic commitment and phenotype maintenance of mesenchymal stem cells *Sci. Rep.* **9** 6891
- [53] Lo Y P, Liu Y S, Rimando M G, Ho J H C, Hui L K and Lee O K 2016 Three-dimensional spherical spatial boundary conditions differentially regulate osteogenic differentiation of mesenchymal stromal cells *Sci. Rep.* **6** 21253